Discrete element modelling and simulation of sand mould manufacture for the lost foam process

Jerzy Rojek[1,*,†], Francisco Zarate[2], Carlos Agelet de Saracibar[2],
Chris Gilbourne[3] and Patrick Verdot[4]

[1]*Institute of Fundamental Technological Research (IPPT), Polish Academy of Sciences, Swietokrzyska 21, 00-049 Warszawa, Poland*
[2]*International Center for Numerical Methods in Engineering (CIMNE), Universidad Politécnica de Cataluña, Campus Norte UPC, 08034 Barcelona, Spain*
[3]*Castings Technology International, 7 East Bank Road, Sheffield, U.K.*
[4]*Huttenes-Albertus France, BP 30309, Z.I. de Pont Brenouille, 60723 Pont Sainte Maxence, CEDEX, France*

SUMMARY

This paper presents a numerical model of mould manufacture for the lost foam casting process. The process of mould filling with sand and sand compaction by vibration are modelled using spherical (in 3D) or cylindrical (in 2D) discrete elements. The motion of discrete elements is described by means of equations of rigid body dynamics. Rigid particles interact among one another with contact forces, both in normal and tangential directions. Numerical simulation predicts defects of the mould due to insufficient sand compaction around the pattern. Combining the discrete element model of sand with the finite element model of the pattern allows us to detect possible distortion of the pattern during mould filling and compaction. Results of numerical simulation are validated by comparison with experimental data. Copyright © 2004 John Wiley & Sons, Ltd.

KEY WORDS: lost foam casting; mould manufacture; discrete element method

1. INTRODUCTION

Lost foam casting (LFC) is a type of metal casting process that uses a sand mould with a polystyrene foam pattern remaining in the mould during metal pouring. The foam pattern is replaced by molten metal, producing the casting. This process gives near net shape castings

---

of high quality and definition and provides a design flexibility not given by other casting technologies, but on the other hand the technology of LFC poses serious difficulties, production of a good mould being one of them.

The production of moulds for LFC process involves three steps. It is started with the placement of the pattern in the moulding box. Next, the pattern is covered with dry and unbonded sand. Then the compaction of the sand is achieved by a vibration process. Once the compaction is complete, the mould is ready to be poured.

Vibratory compaction is one of the most important phases of the LFC process and it may be critical to obtain a good quality cast product. Vibration should ensure uniform and proper compaction, by filling all the cavities with the sand and packing sand to maximum density around the pattern. There is no simple relationship between sand parameters and vibration process parameters, therefore the compaction process is often designed in a purely empirical trial and error manner.

Other defects occurring in the LFC process are the shape defects due to deformation of pattern under sand pressure during filling and the vibration process. This phenomenon has also been studied in our numerical model.

2. BASIC ASSUMPTIONS OF THE NUMERICAL MODEL OF THE MOULDING PROCESS

The objective of the computational model developed is to provide a more rational way to design the filling and compaction process. The main physical phenomenon considered is the flow of granular material (sand) around a rigid or deformable obstacle (moulding box, pattern) under gravity or vibration.

Numerical models of sand compaction adopted in the present study are based on the discrete element method (DEM) which is widely recognized as a suitable tool to model granular materials [1–4]. Within the DEM, it is assumed that the casting sand in the LFC process can be represented as a collection of rigid particles (spheres or balls in 3D and discs in 2D) interacting among themselves in the normal and tangential directions, due to friction.

The material model consisting of rigid spherical elements has been considered the most suitable to model the flow and re-arrangement of the sand grains induced by vibration. It would be difficult to capture properly the main characteristics of such a process using a continuum formulation.

Obviously, it is not intended that each particle used in the DEM represents a sand grain, but it is assumed that the main characteristics of the (loose) sand behaviour during filling and sand compaction can be macroscopically represented using the DEM. On the other hand, it is also obvious that a large number of particles will lead to a better approximation of the results provided by the numerical method used, but a higher computational cost, in terms of computational time and computational resources, is necessary.

Different grain sizes were introduced into our computer model with the size distribution being a function of the sand granulometry.

To allow us to predict the cellular foam pattern deformation during mould filling and compaction the DEM is combined with the finite element method. A general model consists of discrete elements representing sand and finite elements discretising a deformable pattern.

Int. J. Numer. Meth. Engng 2005; **62**:1421–1441

3. DEM FORMULATION

The DEM scheme using spherical rigid elements has been introduced by Cundall [1, 5]. Our study is based on our own implementation of the DEM in the finite element explicit dynamic code Simpact [6, 7]. Combination of the developed discrete element algorithm with finite element method for dynamic analysis of geomechanics problems has been presented in Reference [8].

3.1. Equations of motion

The translational and rotational motion of rigid spherical or cylindrical particles (Figure 1) is described by means of Newton–Euler equations of rigid body dynamics. For the ith element we have

$$m_i \ddot{\mathbf{u}}_i = \mathbf{F}_i \tag{1}$$

$$I_i \dot{\omega}_i = \mathbf{T}_i \tag{2}$$

where $\mathbf{u}$ is the element centroid displacement in a fixed (inertial) co-ordinate frame $\mathbf{X}$, ω – angular velocity, m – element (particle) mass, I – moment of inertia, $\mathbf{F}$ – resultant force, and $\mathbf{T}$ – resultant moment about the central axes. Vectors $\mathbf{F}$ and $\mathbf{T}$ are sums of all forces and moments applied to the ith element due to external load, contact interactions with neighbouring spheres and other obstacles, as well as forces resulting from damping in the system. The form of rotational equation (2) is valid for spheres and cylinders (in 2D) and is simplified with respect to a general form for an arbitrary rigid body with the rotational inertial properties represented by the second order tensor. In general case it is more convenient to describe the rotational motion with respect to co-rotational frame $\mathbf{x}$ which is embedded in each element since in this frame the tensor of inertia is constant. The tensor of inertia for a sphere or cylinder (in 2D) does not change in the fixed global co-ordinate system $\mathbf{X}$, so in this case the rotational motion can be easily considered in this system.
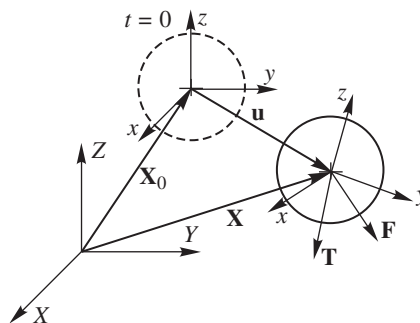

Figure 1. Motion of a rigid particle.

Equations of motion (1) and (2) are integrated in time using a central difference scheme. Time integration operator for the translational motion at the nth time step is as follows:

$$\ddot{\mathbf{u}}_i^n = \frac{\mathbf{F}_i^n}{m_i} \tag{3}$$

$$\dot{\mathbf{u}}_i^{n+1/2} = \dot{\mathbf{u}}_i^{n-1/2} + \ddot{\mathbf{u}}_i^n \Delta t \tag{4}$$

$$\mathbf{u}_i^{n+1} = \mathbf{u}_i^n + \dot{\mathbf{u}}_i^{n+1/2} \Delta t \tag{5}$$

The first two steps in the integration scheme for rotational motion are identical to those given by Equations (3) and (4):

$$\dot{\boldsymbol{\omega}}_i^n = \frac{\mathbf{T}_i^n}{I_i} \tag{6}$$

$$\boldsymbol{\omega}_i^{n+1/2} = \boldsymbol{\omega}_i^{n-1/2} + \dot{\boldsymbol{\omega}}_i^n \Delta t \tag{7}$$

For the rotational plane (2D) motion the rotation angle θ_i can be obtained similarly as displacement vector $\mathbf{u}_i$:

$$\theta_i^{n+1} = \theta_i^n + \omega_i^{n+1/2} \Delta t \tag{8}$$

In three-dimensional motion, rotational position cannot be defined by any vector—rotational velocity $\boldsymbol{\omega}$ cannot be integrated, cf. Reference [9]. The rotation matrix $\boldsymbol{\Lambda}_i$ is used to define the rotational position of the moving frame $\mathbf{x}_i$ with respect to the inertial frame $\mathbf{X}$

$$\mathbf{X} = \boldsymbol{\Lambda}_i \mathbf{x}_i \tag{9}$$

The rotation matrix $\boldsymbol{\Lambda}_i$ is updated according to the following algorithm, cf. References [9, 10]:

$$\Delta \boldsymbol{\theta}_i = \boldsymbol{\omega}_i^{n+1/2} \Delta t \tag{10}$$

$$\Delta \boldsymbol{\Lambda}_i = \cos \|\Delta \boldsymbol{\theta}_i\| \mathbf{1} + \frac{\sin \|\Delta \boldsymbol{\theta}_i\|}{\|\Delta \boldsymbol{\theta}_i\|} \widetilde{\Delta \boldsymbol{\theta}}_i + \frac{1 - \cos \|\Delta \boldsymbol{\theta}_i\|}{\|\Delta \boldsymbol{\theta}_i\|^2} \Delta \boldsymbol{\theta}_i \Delta \boldsymbol{\theta}_i^{\mathrm{T}} \tag{11}$$

$$\boldsymbol{\Lambda}_i^{n+1} = \Delta \boldsymbol{\Lambda}_i \, \boldsymbol{\Lambda}_i^n \tag{12}$$

Here $\Delta \boldsymbol{\theta} = \{\Delta \theta_x \ \Delta \theta_y \ \Delta \theta_z\}^{\mathrm{T}}$ denotes the vector of incremental rotation, $\Delta \boldsymbol{\Lambda}$ is the incremental rotation matrix, and $\widetilde{\Delta \boldsymbol{\theta}}$ is the skew-symmetric matrix defined as

$$\widetilde{\Delta \boldsymbol{\theta}} = \begin{bmatrix} 0 & -\Delta \theta_z & \Delta \theta_y \\ \Delta \theta_z & 0 & -\Delta \theta_x \\ -\Delta \theta_y & \Delta \theta_x & 0 \end{bmatrix} \tag{13}$$

It must be remarked that knowledge of the rotational configuration is not always necessary. If tangential forces are calculated incrementally, then knowledge of the vector of incremental rotation $\Delta\boldsymbol{\theta}$ is sufficient. Then steps (11) and (12) are not necessary which saves considerable computational cost of the time integration scheme.

3.2. Evaluation of contact forces

Once the contact for a pair of particles has been detected, the forces occurring at the contact point are calculated. The interaction between the two bodies can be represented by the contact forces $\mathbf{F}_1$ and $\mathbf{F}_2$, which, by the Newton's third law, will satisfy the following relationship:

$$\mathbf{F}_1 = -\mathbf{F}_2 \tag{14}$$

We take $\mathbf{F} = \mathbf{F}_1$ and decompose $\mathbf{F}$ into normal and tangential components, $\mathbf{F}_n$ and $\mathbf{F}_T$, respectively (Figure 2)

$$\mathbf{F} = \mathbf{F}_n + \mathbf{F}_T = F_n\mathbf{n} + \mathbf{F}_T$$

where $\mathbf{n}$ is the unit vector normal to the particle surface at the contact point (this implies that it lies along the line connecting the centers of the two particles) and directed outwards from the particle 1.

The contact forces F_n and $\mathbf{F}_T$ are obtained using a constitutive model formulated for the contact between two rigid spheres (Figure 3). The contact interface in our formulation is characterized by the normal and tangential stiffness k_n and k_T, the Coulomb friction coefficient μ, and the contact damping coefficient c_n.

The damping is used to dissipate kinetic energy and to decrease oscillations of the contact forces. It is assumed to contribute to the normal contact force. Thus, we can decompose the normal contact force F_n to the elastic part F_{ne} and to the damping contact force F_{nd}

$$F_n = F_{ne} + F_{nd} \tag{15}$$

The elastic part of the normal contact force F_{ne} is proportional to the normal stiffness k_n and the penetration of the two particle surfaces u_{rn}
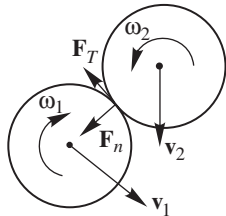
$$F_{ne} = k_n u_{rn} \tag{16}$$

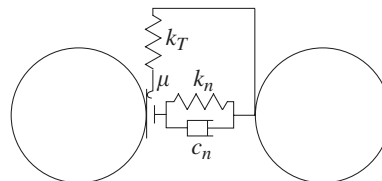Figure 2. Decomposition of the contact force.

Figure 3. Model of the contact interface.

The penetration is calculated as

$$u_{rn} = d - r_1 - r_2 \tag{17}$$

where d is the distance of the particle centres, and r_1, r_2 their radii. In the formulation used in the present study no cohesion is allowed, so no tensile normal contact forces are allowed

$$F_{ne} \leqslant 0 \tag{18}$$

If $u_{rn} < 0$, formula (16) is valid, otherwise $F_{ne} = 0$.

The contact damping force is assumed to be of viscous type

$$F_{nd} = c_n v_{rn} \tag{19}$$

proportional to the normal relative velocity v_{rn} of the centres of the two particles in contact

$$v_{rn} = (\dot{\mathbf{u}}_2 - \dot{\mathbf{u}}_1) \cdot \mathbf{n} \tag{20}$$

The value of damping c_n can be taken as a fraction of the critical damping C_{cr} for the system of two rigid bodies with masses m_1 and m_2, connected with a spring of the stiffness k_n (cf. Reference [11])

$$C_{\mathrm{cr}} = 2\sqrt{\frac{m_1 m_2 k_n}{m_1 + m_2}} \tag{21}$$

The tangential reaction $\mathbf{F}_T$ is brought about by friction opposing the relative motion at the contact point. The relative tangential velocity at the contact point $\mathbf{v}_{rT}$ is calculated from the following relationship

$$\mathbf{v}_{rT} = \mathbf{v}_r - \mathbf{v}_r \cdot \mathbf{n} \tag{22}$$

$$\mathbf{v}_r = (\dot{\mathbf{u}}_2 + \boldsymbol{\omega}_2 \times \mathbf{r}_{c2}) - (\dot{\mathbf{u}}_1 + \boldsymbol{\omega}_1 \times \mathbf{r}_{c1}) \tag{23}$$

where $\dot{\mathbf{u}}_1$, $\dot{\mathbf{u}}_2$, and $\boldsymbol{\omega}_1$, $\boldsymbol{\omega}_2$ are the translational and rotational velocities of the particles, and $\mathbf{r}_{c1}$ and $\mathbf{r}_{c2}$ are the vectors connecting particle centres with contact points.

The relationship between the friction force $\|\mathbf{F}_T\|$ and relative tangential u_{rT} displacement for the classical Coulomb model (for a constant normal force F_n) is shown in Figure 4(a). This relationship would produce non-physical oscillations of the friction force in the numerical solution due to possible changes of the direction of sliding velocity. To prevent this the Coulomb friction model must be regularized. A possible regularization procedure involves decomposition of the tangential relative velocity into a reversible and irreversible parts, $\mathbf{v}_{rT}^{\mathrm{r}}$ and $\mathbf{v}_{rT}^{\mathrm{ir}}$, respectively:

$$\mathbf{v}_{rT} = \mathbf{v}_{rT}^{\mathrm{r}} + \mathbf{v}_r^{\mathrm{ir}} \tag{24}$$

This is equivalent to formulation of the frictional contact as a problem analogous to that of elastoplasticity, which can be seen clearly from the friction force–tangential displacement relationship in Figure 4(b). This analogy allows us to calculate the friction force employing the radial return algorithm analogous to that used in elastoplasticity. First a trial state is calculated

$$\mathbf{F}_T^{\mathrm{trial}} = \mathbf{F}_T^{\mathrm{old}} - k_T \mathbf{v}_{rT} \Delta t \tag{25}$$
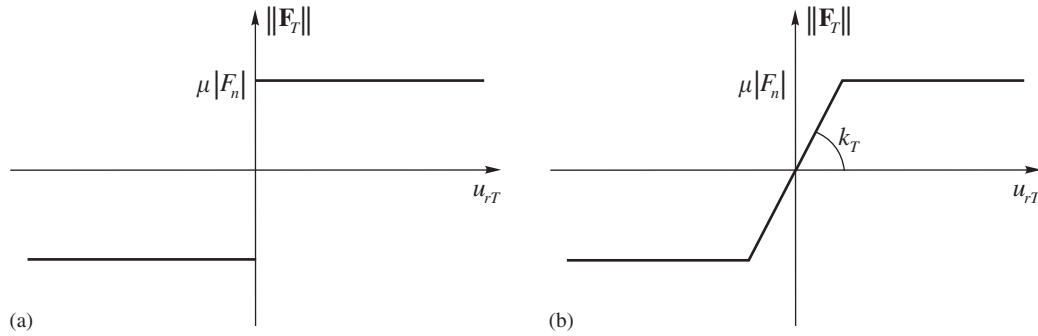
Figure 4. Friction force vs relative tangential displacement: (a) Coulomb
law; and (b) regularized Coulomb law.

and then the slip condition is checked

$$\phi^{\text{trial}} = \|\mathbf{F}_T^{\text{trial}}\| - \mu|F_n| \tag{26}$$

If $\phi^{\text{trial}} \leqslant 0$, we have the case of stick contact and the friction force is assigned the trial value

$$\mathbf{F}_T^{\text{new}} = \mathbf{F}_T^{\text{trial}} \tag{27}$$

otherwise (slip contact) a return mapping is performed

$$\mathbf{F}_T^{\text{new}} = \mu|F_n| \frac{\mathbf{F}_T^{\text{trial}}}{\|\mathbf{F}_T^{\text{trial}}\|} \tag{28}$$

3.3. Rolling resistance

The sliding friction cannot provide any resistance to the movement of the sphere (cylinder) rolling on a rough surface if there is no relative tangential velocity at the contact point ($v_{rT} = 0$). The rolling resistance can be simulated numerically by applying the rolling contact moment

$$M = f|F_n| \tag{29}$$

which appears due to the eccentricity f of the normal reaction F_n (Figure 5). The distance f is sometimes called the coefficient of rolling friction. It depends on the deformation of the two contacting surfaces, exact solution of such a problem would require taking into account material properties, geometry and acting forces. In the present formulation dependence of the coefficient of rolling friction f on the element size is taken into account by the assumption

$$f = r \tan \alpha \tag{30}$$

with r being the element radius and the angle α treated as a constant parameter.

The rolling friction is extended to the interparticular contact where the moment M resists the relative rotation of the two particles
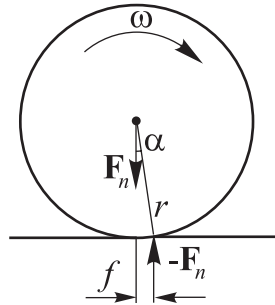
$$\omega_r = \omega_1 - \omega_2 \tag{31}$$

Figure 5. Resisting moment due to the eccentricity of the normal reaction.

The coefficient of the rolling friction is taken as dependent on the size of the smaller one of the two particles

$$f = r_{\min} \tan \alpha \tag{32}$$

where

$$r_{\min} = \min(r_1, r_2) \tag{33}$$

Expression (29) for the rolling resisting moment is analogical to the Coulomb friction law, and similarly to the Coulomb friction law it must be regularized when implemented in the numerical algorithm.

3.4. Background damping

A quasi-static state of equilibrium of the assembly of particles can be achieved by application of adequate damping. Described previously contact damping is a function of the relative velocity of the contacting body. It is sometimes necessary to apply damping for non-contacting particles to dissipate their energy. There are two types of such damping, referred here as background, implemented in our formulation, one of viscous type and the other of non-viscous type. In both cases damping terms $\mathbf{F}_i^{\mathrm{damp}}$ and $\mathbf{T}_i^{\mathrm{damp}}$ are added to equations of motion (1) and (2)

$$m_i \ddot{\mathbf{u}}_i = \mathbf{F}_i + \mathbf{F}_i^{\mathrm{damp}} \tag{34}$$

$$I_i \dot{\boldsymbol{\omega}}_i = \mathbf{T}_i + \mathbf{T}_i^{\mathrm{damp}} \tag{35}$$

with damping terms given by

- for viscous damping

$$\mathbf{F}_i^{\mathrm{damp}} = -\alpha^{\mathrm{vt}} m_i \dot{\mathbf{u}}_i \tag{36}$$

$$\mathbf{T}_i^{\mathrm{damp}} = -\alpha^{\mathrm{vr}} I_i \boldsymbol{\omega}_i \tag{37}$$

- for non-viscous damping

$$\mathbf{F}_i^{\mathrm{damp}} = -\alpha^{\mathrm{nvt}} \|\mathbf{F}_i\| \frac{\dot{\mathbf{u}}_i}{\|\dot{\mathbf{u}}_i\|} \tag{38}$$

$$\mathbf{T}_i^{\mathrm{damp}} = -\alpha^{\mathrm{nvr}} \|\mathbf{T}_i\| \frac{\boldsymbol{\omega}_i}{\|\boldsymbol{\omega}_i\|} \tag{39}$$

where α^{vt}, α^{vr}, α^{nvt} and α^{nvr} are respective damping constants. It can be seen from Equations (36)–(39) that non-viscous like viscous damping is opposite to velocity, the difference consists in the evaluation of the magnitude of damping force–viscous damping is proportional to the magnitude of velocity, while non-viscous damping is proportional to the magnitude of resultant force and moment.

3.5. Numerical stability

Explicit integration in time yields high computational efficiency. Therefore the method enables us to analyse large models. The known disadvantage of the explicit integration scheme is its conditional numerical stability imposing the limitation on the time step Δt. The time step Δt must not be larger than a critical time step Δt_{cr}

$$\Delta t \leqslant \Delta t_{cr} \tag{40}$$

determined by the highest natural frequency of the system $\omega_{\max}$

$$\Delta t_{cr} = \frac{2}{\omega_{\max}} \tag{41}$$

If damping exists, the critical time increment is given by

$$\Delta t_{cr} = \frac{2}{\omega_{\max}} \left(\sqrt{1 + \xi^2} - \xi \right) \tag{42}$$

where ξ is the fraction of the critical damping corresponding to the highest frequency $\omega_{\max}$. Exact determination of the highest frequency $\omega_{\max}$ would require a solution of the eigenvalue problem defined for the whole system of connected rigid particles. In an approximate solution procedure, eigenvalue problems can be defined separately for every rigid particle using the linearized equations of motion

$$\mathbf{m}_i \ddot{\mathbf{r}}_i + \mathbf{k}_i \mathbf{r}_i = \mathbf{0} \tag{43}$$

where

$$\mathbf{m}_i = \{m_i \ \ m_i \ \ m_i \ \ I_i \ \ I_i \ \ I_i\}^{\mathrm{T}}, \quad \mathbf{r}_i = \{(u_x)_i \ \ (u_y)_i \ \ (u_z)_i \ \ (\theta_x)_i \ \ (\theta_y)_i \ \ (\theta_z)_i\}^{\mathrm{T}} \tag{44}$$

and $\mathbf{k}_i$ is the stiffness matrix accounting for the contributions from all the penalty constraints active for the ith particle. Equation (44) defines the vectors $\mathbf{m}_i$ and $\mathbf{r}_i$ for a spherical particle in three-dimensional space. For a cylindrical particle in a two-dimensional model the respective vectors are defined as follows:

$$\mathbf{m}_i = \{m_i \ \ m_i \ \ I_i\}^{\mathrm{T}}, \quad \mathbf{r}_i = \{(u_x)_i \ \ (u_y)_i \ \ (\theta_z)_i\}^{\mathrm{T}} \tag{45}$$

Equation (43) leads to an eigenproblem

$$\mathbf{k}_i \mathbf{r}_i = \lambda_j \mathbf{m}_i \mathbf{r}_i \qquad (46)$$

where eigenvalues λ_j ($j = 1, \ldots, 6$ in 3D case, and $j = 1, 2, 3$ for 2D case) are the squared frequencies of free vibrations:

$$\lambda_j = \omega_j^2 \qquad (47)$$

In a 3D problem, three of six frequencies ω_j are translational, and the other three-rotational.

In the algorithm implemented, a further simplification is assumed. The maximum frequency is estimated as the maximum of natural frequencies of mass–spring systems defined for all the particles with one translational and one rotational degree of freedom. The translational and rotational free vibrations are governed by the following equations:

$$m_i \ddot{u}_n + k_n u_n = 0 \qquad (48)$$

$$I_i \ddot{\theta} + k_\theta \theta = 0 \qquad (49)$$

where it is assumed that the translational motion is due to the contact interaction in the normal direction (the spring stiffness k_n represents the penalty stiffness in the normal direction), and the rotational stiffness is due to the contact stiffness (penalty) in the tangential direction. Given the tangential penalty k_T, it can be shown that the rotational stiffness k_θ can be obtained as

$$k_\theta = k_T r^2 \qquad (50)$$

where r is the length of the vector connecting the mass centre to the contact point.

The natural frequency of the translational vibrations is given by the following equation:

$$\omega_n = \sqrt{\frac{k_n}{m_i}} \qquad (51)$$

while the rotational frequency ω_θ can be obtained from the formula

$$\omega_\theta = \sqrt{\frac{k_\theta}{I_i}} \qquad (52)$$

With the rotational inertia of a sphere

$$I = \tfrac{2}{5} m r^2 \qquad (53)$$

and k_θ given by Equation (50), the rotational frequency can be calculated as

$$\omega_\theta = \sqrt{\frac{5 k_T}{2 m_i}} \qquad (54)$$

If $k_T = k_n$, the rotational frequency ω_θ is considerably higher than the translational frequency ω_n obtained from Equation (51), which results in a smaller critical time increment, cf. Equation (41). To avoid the determination of a critical time step by the rotational frequencies, the rotational inertia terms are scaled adequately. The concept of scaling rotational inertia terms is commonly used for shell elements, cf. Reference [12].

3.6. Contact search algorithm

Changing contact pairs of elements during the analysis process must be automatically detected. The simple ('brute-force') approach to identify interaction pairs by checking every sphere against every other sphere would be very inefficient, with the computational time proportional to n^2 (of order $O(n^2)$), where n is the number of elements.

A number of more effective methods has been developed to determine the particle interaction. An overview of contact detection methods developed for discrete element method can be found in References [4, 13]. In usually used contact detection schemes prior to the contact resolution objects are spatially ordered using an appropriate sorting algorithm, cf. Reference [4]. Spatial sorting enables efficient determination of neighbouring objects, so the subsequent contact check can be limited to the pairs of objects lying close to each other.

Various spatial sorting algorithms are known. Most popular of them can be classified into following groups, cf. References [4, 13]:

- grid subdivision
- binary trees
- quad-trees (in 2D) and octrees (in 3D)
- body based cells
- spatial heapsort

In our formulation the contact search is based on the quad-tree and octree sorting coupled with the body based cell technique.

Building octree or quad-tree structures at every time step can be quite expensive. Since time steps are very small, most of contacting pairs can be the same as those in the previous step. Using the information about contact pairs existing in the previous step can speed up the contact search. Therefore the algorithm of contact detection scheme consists of two stages: (i) global search, identifying the pairs of potential contacts, based on the quadtree and octree sorting, (ii) local search, verifying the list of potential contacts (typical for body based cell algorithm).

3.7. Density evaluation

One of the main results of interest in the simulation of filling and compaction by vibration of the sand in the Lost Foam modelling is the distribution of density. To evaluate the density map using the discrete element method an algorithm has been developed. For each particle a control volume is defined as it is shown in Figure 6. Then the average local density is evaluated as the apparent density of a porous material defined according to the following expressions:

$$\bar{\rho}^{(i)} = \rho \frac{V_c - V_0^{(i)}}{V_c}, \quad V_0^{(i)} = V_c - V_i - \sum_j \bar{V}_j^{(i)} \tag{55}$$

where $\bar{\rho}^{(i)}$ is the apparent local density of a porous material evaluated at the neighbourhood of the ith particle, ρ is the real density of the particle material, V_c is the control volume associated with the i-particle, V_i is the volume of the ith particle, $V_0^{(i)}$ is the volume of pores in the control volume established for the i-particle, $\bar{V}_j^{(i)}$ is the volume of the intersection of the jth particle with the control volume.

In the computation of the apparent average density associated to a particle, the intersection (common part) of the control volume with the volumes of interacting particles has been
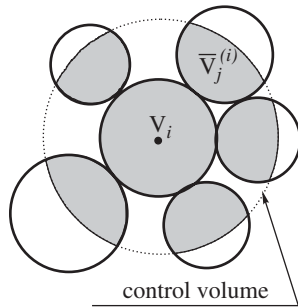
Figure 6. Definition of the control volume for density evaluation.
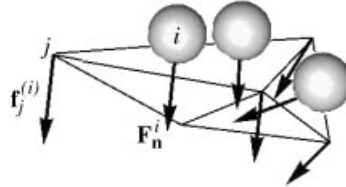

Figure 7. Evaluation of contact forces and average contact pressure.

computed using exact analytical expression. Value of the local apparent density depends on the control domain volume, big domain volumes lead to uniform distribution of local apparent density, small domain volume can overestimate or underestimate the value of the apparent density. In the results presented in the paper the control volume has been defined as the sphere of the radius equal $2R_{\max}$, where $R_{\max}$ is the maximum particle radius of all the particles.

3.8. Contact pressure evaluation

Contact pressure exerted by the sand on the pattern is another of the main results of interest in the moulding process. Figure 7 shows a part of the outer surface of the pattern with some contacting sand particles. This figure illustrates schematically how the pressure is calculated from node-segment contact interaction. The pressure is computed using the following formulae:

$$\bar{p}^j = \frac{\sum \mathbf{f}_j^{(i)}}{A_j}, \quad \mathbf{f}_j^{(i)} = H_j \mathbf{F}_n^i \tag{56}$$

where $\bar{p}^j$ is the average pressure evaluated at the jth node, $\mathbf{f}_j^{(i)}$ is the force at the jth node resulting from the normal contact force $\mathbf{F}_n^i$ between the ith particle and a surface segment connected to the jth node, and H_j is the shape function used to distribute the contact forces from the contact point to the segment nodes corresponding to the jth node.

3.9. Simulation of vibration process

In the computational simulation of the dynamics of the vibration process, the equations of motion can be described relatively to a fixed system of reference $\mathbf{X}$ (cf. Figure 8),

$$\mathbf{M}\ddot{\mathbf{X}} = \mathbf{F} \tag{57}$$

or alternatively, relative to a moving $\mathbf{x}$ system fixed to the vibrating box,

$$\mathbf{M}\ddot{\mathbf{x}} = \mathbf{F} - \mathbf{M}\ddot{\mathbf{s}} \tag{58}$$
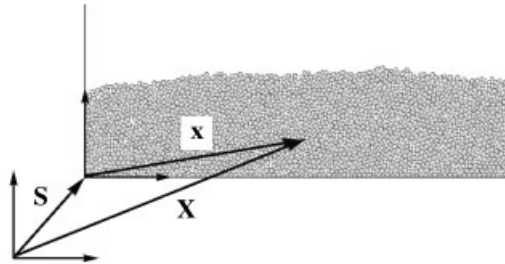
Figure 8. Motion equations in a fixed and moving (fixed to the box) system.

4. NUMERICAL EXAMPLES

The computational model developed by CIMNE has been implemented in an enhanced version of the 'in house' developed explicit dynamic computer code SIMPACT. SIMPACT is an explicit dynamic computer code mainly developed to simulate contact and impact dynamic problems. Further developments on the code have been necessary in order to deal with the computational simulation of the moulding process.

The numerical model described in the previous section has been implemented in a computer program. Different computational simulations have been performed in order to assess the formulation developed for the sand flow and compaction by vibration within the lost foam technology. Here four simulation tests are considered. In the first test, the repose angle was evaluated. In the second example the flow of sand into horizontal tube under vibration was studied. Third example shows the possibility to study deformation of the pattern under sand pressure during mould filling and vibration. The last example presents possibilities of 3D simulation for a test pattern geometry. Numerical results are compared with experimental data.

4.1. Repose angle test

Simple experiments of emptying a small hopper have been carried out to obtain the repose angle of different sand types. Experiments yielded the repose angle values ranging from 25 to 36°. Two of the sand configurations discharged from a small hopper are shown in Figure 9. The lowest values of repose angle, 25–26° correspond to the cerabead, an artificial sand characterized by perfectly rounded grains.

This test has been used to calibrate parameters of the numerical model of sand yielding required repose angles which is thought to be the most important factor controlling sand flow during the mould filling and compaction.

A 2D numerical model has been created to reproduce the experiments. The sand has been represented by 10 700 particles of different size, their diameters ranging from 1 to 4.5 mm and size distribution according to the granulometry of one of the real sands tested. The particle size has been scaled 4 times with respect to sand grain size.

Figure 10 shows the computational results obtained using the following parameters: mass density $\rho = 2400 \, \text{kg/m}^3$, inter-particle contact normal and tangential stiffness $k_n = k_T = 7 \times 10^4 \, \text{N/m}$, Coulomb friction coefficient $\mu = 0.8$, contact damping $\xi = 1.0$ (equal to the critical damping), rigid wall-particle contact characterized with $k_n = k_T = 2 \times 10^4 \text{N/m}$, Coulomb
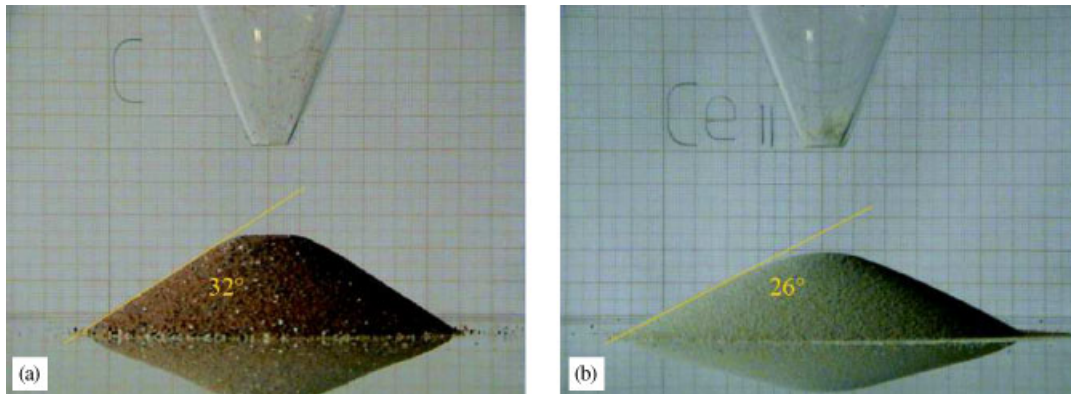
Figure 9. Experimental repose angle: (a) sand used in the foundry of Castings Technology International (England); and (b) artificial sand cerabead.
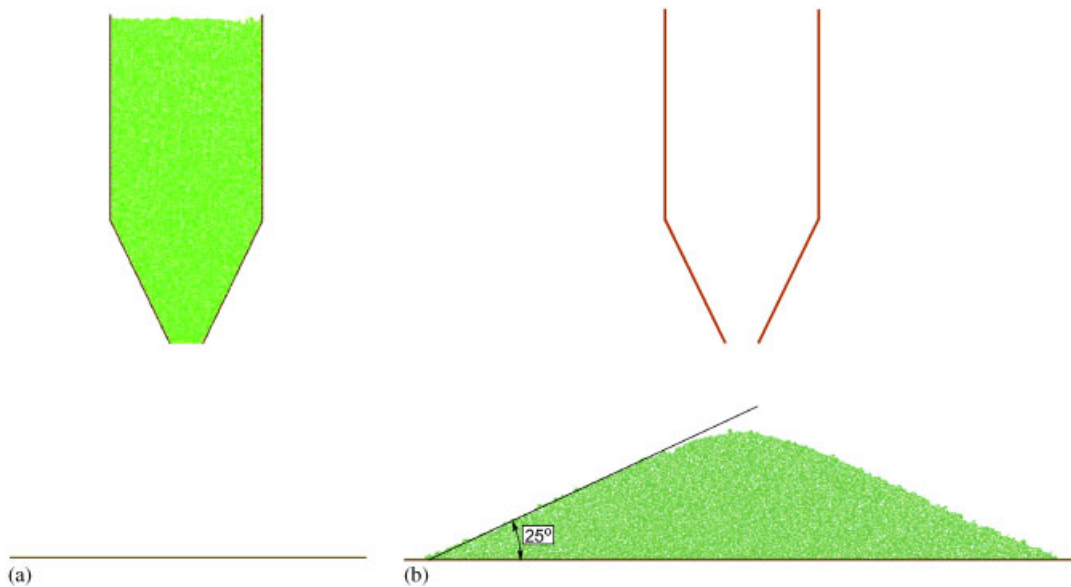

Figure 10. Numerical simulation of the repose angle test: (a) initial configuration; and (b) final configuration.

friction coefficient $\mu = 0.35$, contact damping $\xi = 0.95$, and rolling resistance parameter a was assumed 0.1 of the particle radii. Small background damping was taken using $\alpha^{nvt} = 0.03$ and $\alpha^{nvr} = 0.3$. The repose angle obtained, 25°, is close to the experimental results. It agrees especially well with the value for the cerabead sand.

Different analysis have been made using different model features and changing the parameter values to assess their influence on the repose angle. Sliding and rolling friction between particles
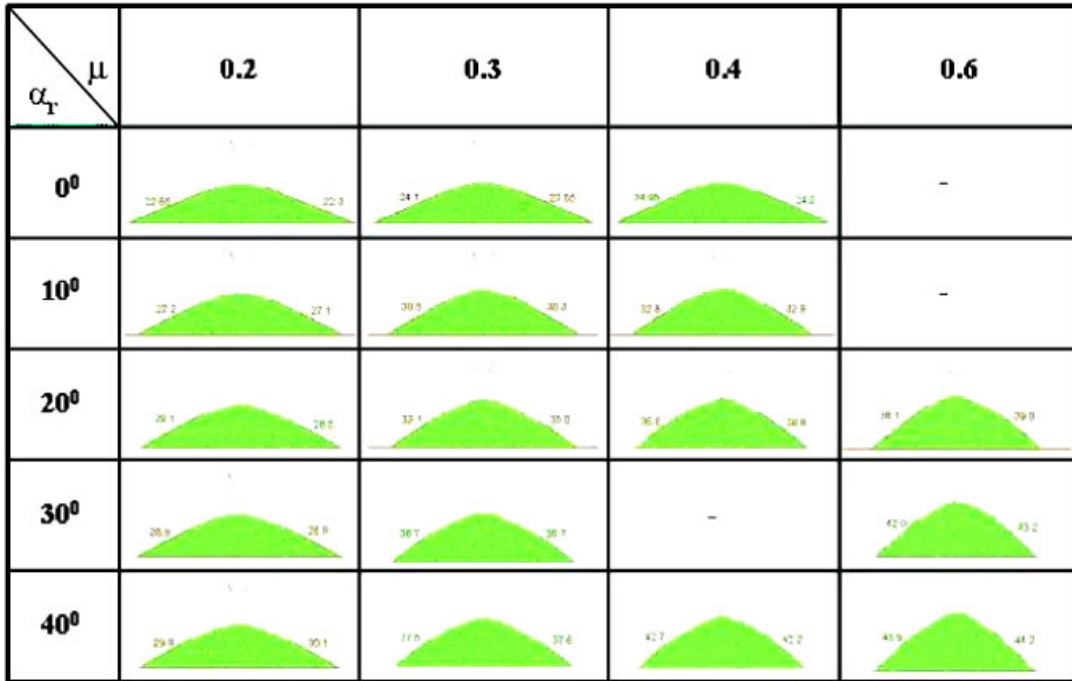
Figure 11. Repose angle values for different values of sliding and rotational friction.

have been found the most important factors influencing the sand repose angle. The results of the study are presented in Figures 11 and 12 in the forms of the table and contour map. The contour map in Figure 12 can be used to assume adequate sliding and rolling friction parameters for sand with characterized with a given value of repose angle. As it can be seen from the map there is not unique solution for this and established the procedure to adopt a given value of rolling friction, for instance characterized with the angle $\alpha = 10°$ and then take a corresponding value of the Coulomb friction coefficient.

4.2. Sand flow into horizontal tubes

A metal test piece consisting of a series of three tubes of different diameters (Figure 13) was placed in the sand box. The box was filled and vibrated in the vertical direction, with vibration frequency being 50 Hz and acceleration amplitude of 1.5 G. Migration of the sand into the horizontal tubes has been investigated. The results of experiments for different vibration periods are shown in Figure 14.

Numerical simulation of this test has been carried out using 2D model with the tube of largest diameter considered only. The model employed particles of the same characteristics as those used in the previous example. Results of numerical analysis are shown in Figure 15. A good correlation of the numerical results with the experimental ones can be observed.

This example has been used to study the influence of the vibration frequency on the effectiveness of the sand flow. The effectiveness of the sand flow was measured by the volume
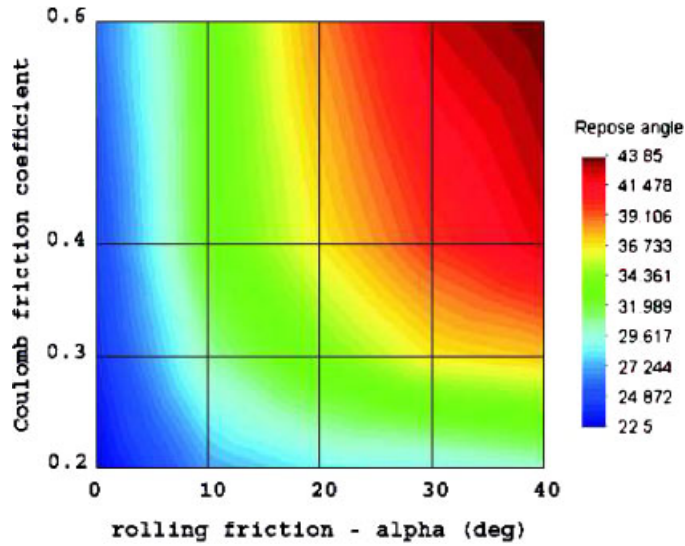
Figure 12. Map of the repose angle values in function of sliding and rotational friction.
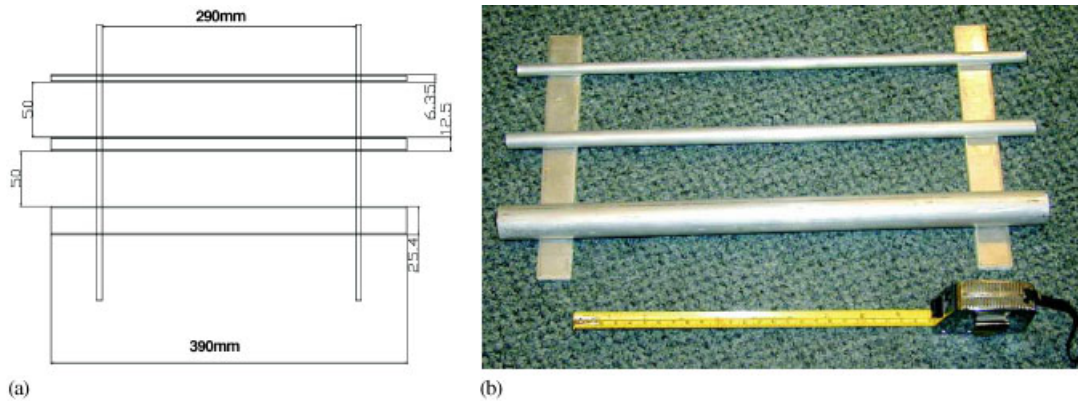

Figure 13. Metal tubes: (a) geometry definition; and (b) view of the tubes.

of the sand inside the tube. The results of the study showing volumes obtained with different frequencies at different time instants. The maximum volume has been found for the frequency of 65 Hz, the value obtained in the experiments was slightly higher that is 85 Hz (Figure 16).

4.3. Test with a L-shaped pattern

Distortion of a simple L-shaped pattern during filling and vibration has been studied experimentally and numerically. Experimental results show that the filling process distorts the pattern (Figure 17(a)) and that an area of low sand density exists below the horizontal section. The
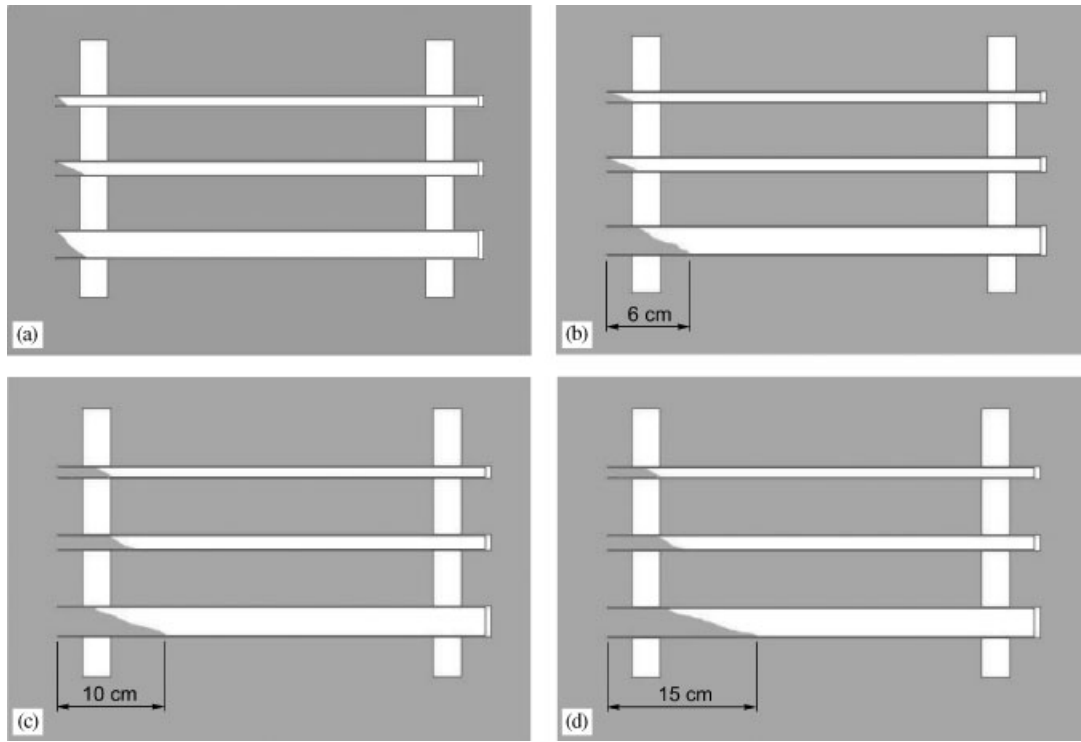
Figure 14. Sand flow into horizontal tubes under vibration—experimental results: (a) $t = 0$s; (b) $t = 5$ s; (c) $t = 20$ s; and (d) $t = 40$ s.

pattern distortion although slightly reduced is still observed after vibration (Figure 18(a)). During vibration the sand flows into the cavity below the horizontal part of the pattern.

Similar distortion of the pattern during filling and compaction has been predicted by numerical analysis, cf. Figures 17(b) and 18(b). Numerical simulation has been carried out using a 2D model of similar sand characteristics as those used in the two examples above. The pattern has been discretized with 4-node plain strain elements. Elastic properties of the polystyrene were characterized by Young's modulus $E = 6.4$ MPa and Poisson coefficient $v = 0.35$, its density $\rho = 12$ kg/m^3.

Figures 17 and 18 demonstrate a very good agreement of the pattern distortion obtained in experiments and numerical simulation.

4.4. 3D test of layer-wise mould filling and compaction

Experimental study and 3D numerical analysis of mould filling and compaction have been carried out for a simple disc shape with a side bracket shown in Figure 19. This design was chosen as being able to characterise basic problems encountered in industrial LFC processes.

Sand was filled in layers and vibrated during filling. In order to validate the simulation of sand flow around the pattern, experimental trials were performed using coloured sand containing a chemical binder. Figure 20(a) shows a section through the sand block revealing the test pattern
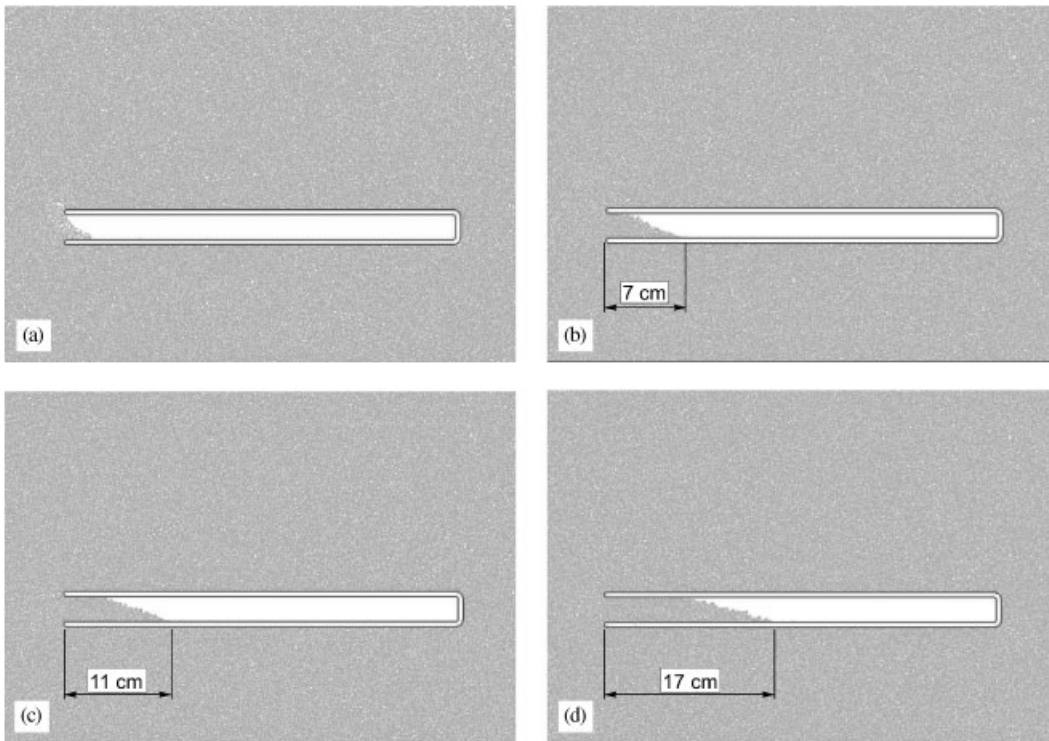
Figure 15. Sand flow into horizontal tubes under vibration—numerical results: (a) $t = 0$ s;
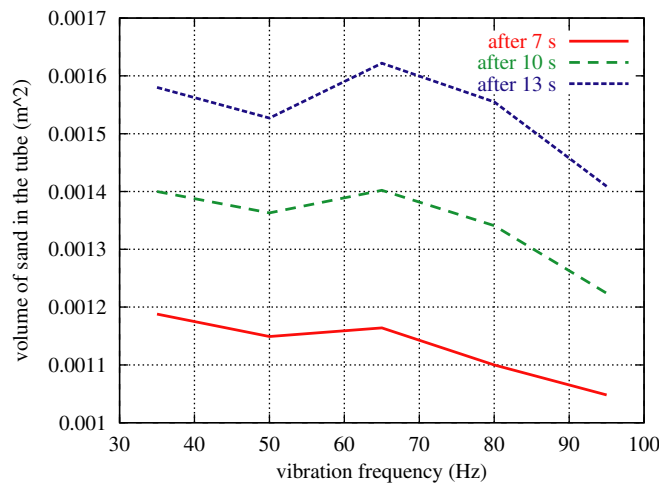(b) $t = 5$ s; (c) $t = 20$ s; and (d) $t = 40$ s.

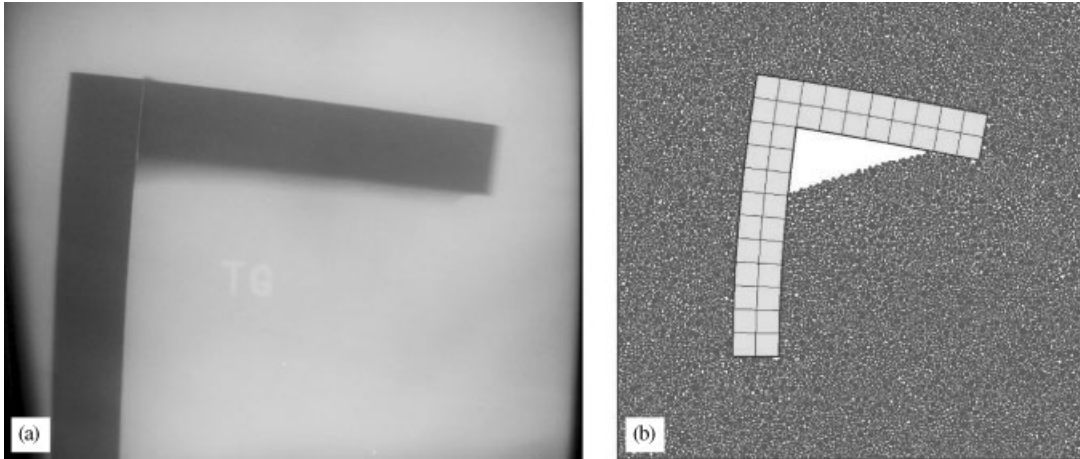Figure 16. Sand flow effectiveness in function of the vibration frequency.

Figure 17. Deformation of the foam pattern after mould filling:
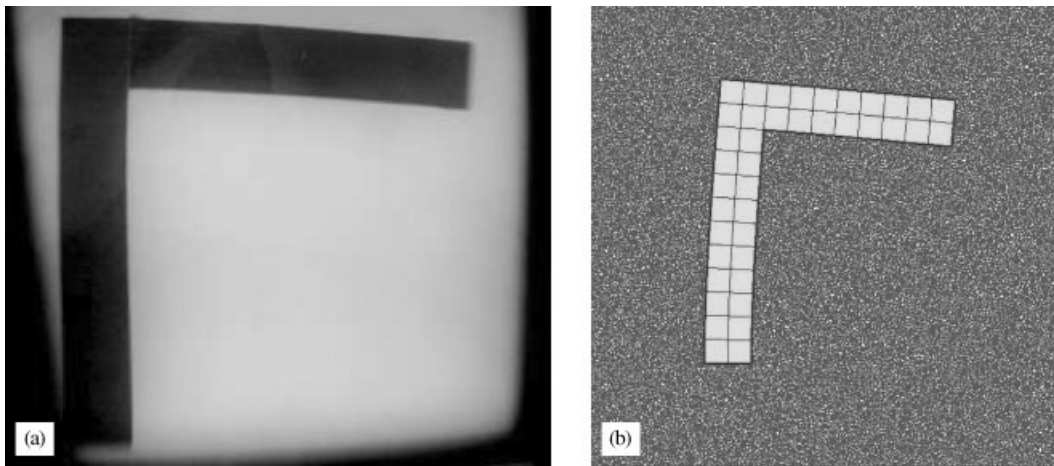(a) experiment; and (b) numerical simulation.

Figure 18. Deformation of the foam pattern after vibration:
(a) experiment; and (b) numerical simulation.

and sand layers. Similar sand flow around the pattern has been obtained in numerical simulation (Figure 20(b)).

This example demonstrates the computational effectiveness of the numerical model and the possibility to treat large models—in this case nearly 180 000 particles have been used.
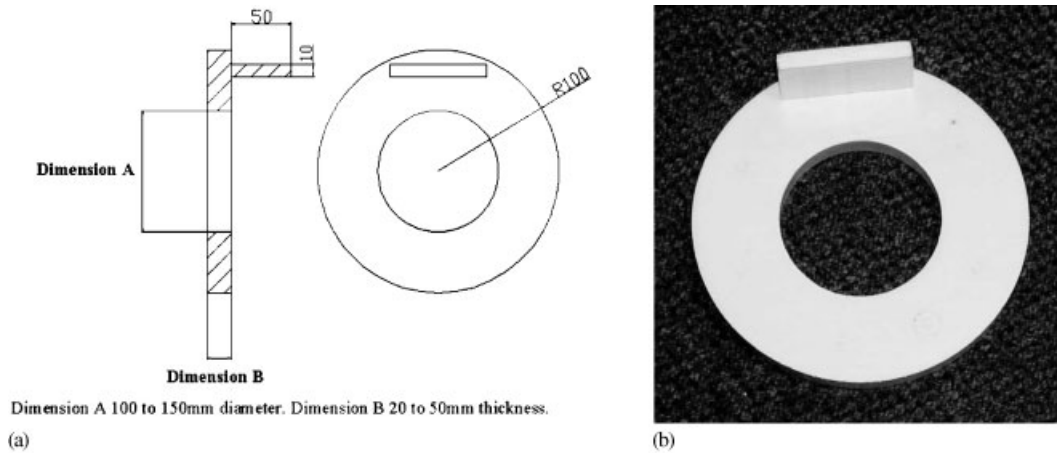
Figure 19. 3D test of moulding process: (a) design of the test casting; and (b) the foam pattern.
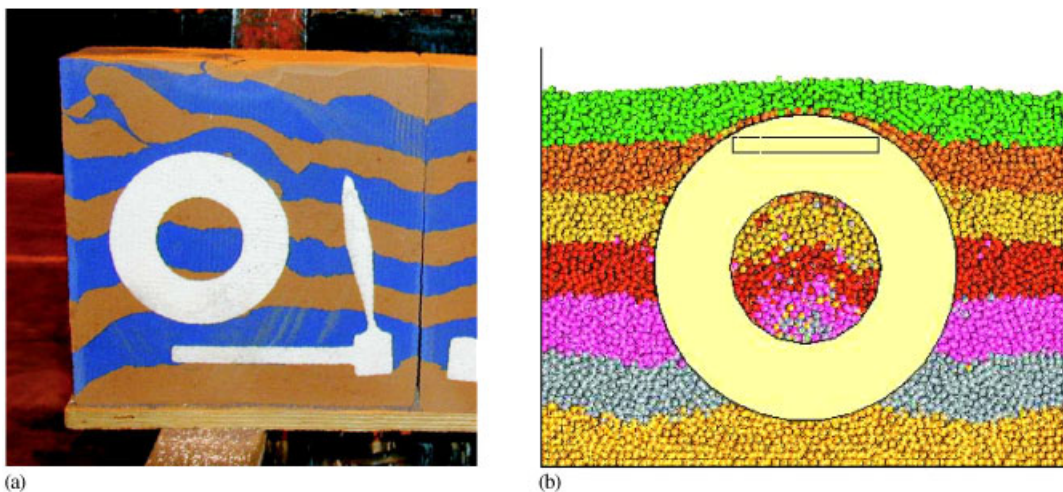

Figure 20. Sand layers: (a) experiment; and (b) numerical simulation.

5. CONCLUSIONS

The following conclusions may be obtained:

- A numerical model based on the discrete element method (DEM) using spherical or cylindrical rigid particles is suitable to model mould manufacture, sand filling and compaction of sand by vibration.
- Computer implementation within the FE explicit dynamic code enables us to create a model combining the DEM with the finite element method, which gives the possibility to take into account deformation of the foam pattern during filling and vibration.
- Experimental validation tests show good correlation of numerical results with practice.

- Numerical analysis can be used to find parameters characterizing mould manufacture process.

REFERENCES

1. Cundall PA, Strack ODL. A discrete numerical method for granular assemblies. *Geotechnique* 1979; **2**:47–65.
2. Campbell CS. Rapid granular flows. *Annual Review of Fluid Mechanics* 1990; **2**:57–92.
3. Mustoe G (ed.). *Engineering Computation* 1992; **9**(2), (Special issue).
4. Williams J, O'Connor R. Discrete element simulation and contact problem. *Archives of Computer Methods in Engineering* 1999; **6**(4):279–304.
5. Cundall PA. Formulation of a three dimensional distinct element model—Part I. A scheme to detect and represent contacts in a system of many polyhedral blocks. *International Journal of Rock Mechanics Mineral Science and Geomechanics Abstracts* 1988; **25**(3):107–116.
6. Rojek J, Oate E, Zarate F, Miquel J. Modelling of rock, soil and granular materials using spherical elements. *2nd European Conference on Computational Mechanics ECCM-2001*, Cracow, 26–29 June 2001.
7. Simpact. http://www.quantech.es/simpact.htm.
8. Oñate E, Rojek J. Combination of discrete element and finite element methods for dynamic analysis of geomechanics problems. *Computer Methods in Applied Mechanics and Engineering* 2004; **193**:3087–3128.
9. Argyris J. An excursion into large rotations. *Computer Methods in Applied Mechanics and Engineering* 1982; **32**:85–155.
10. Benson DJ, Hallquist JO. A simple rigid body algorithm for structural dynamics programs. *International Journal for Numerical Methods in Engineering* 1986; **12**:723–749.
11. Taylor LM, Preece DS. Simulation of blasting induced rock motion. *Engineering Computation* 1992; **9**(2):243–252.
12. Hughes TJR. *The Finite Element Method. Linear Static and Dynamic Analysis*. Prentice-Hall: Englewood Cliffs, NJ, 1987.
13. Löhner R. *Applied CFD Techniques. An Introduction based on Finite Element Methods*. Wiley: New York, 2001.